

# Supporting Information

## Impurity Tracking Enables Enhanced Control and Reproducibility of Hybrid Perovskite Vapour Deposition

Juliane Borchert,<sup>†</sup> Ievgen Levchuk,<sup>‡,¶</sup> Lavina C. Snoek,<sup>†</sup> Mathias Uller Rothmann,<sup>†</sup> Renée Haver,<sup>§</sup> Henry J. Snaith,<sup>†</sup> Christoph J. Brabec,<sup>‡,||</sup> Laura M. Herz,<sup>†</sup> and Michael B. Johnston<sup>\*,†</sup>

<sup>†</sup>*Clarendon Laboratory, Department of Physics, University of Oxford, Parks Road, OX1 3PU, United Kingdom*

<sup>‡</sup>*Materials for Electronics and Energy Technology (i-MEET) Friedrich-Alexander-Universität Erlangen-Nürnberg Martensstraße 7, 91058 Erlangen, Germany*

<sup>¶</sup>*Energy Campus Nürnberg (EnCN) Fürther Str. 250, 90429 Nürnberg, Germany*

<sup>§</sup>*Department of Chemistry, University of Oxford, Chemistry Research Laboratory, Oxford OX1 3TA, United Kingdom*

<sup>||</sup>*FZ Jülich, HI-ErN (IEK-11), Erlangen, Immerwahrstrasse 2, D-91058 Erlangen, Germany*

E-mail: michael.johnston@physics.ox.ac.uk

# 1 Further Precursor Information

## 1.1 MAI precursor

*High-purity methylammonium iodide* was synthesized by mixing HI and methylamine ( $\text{CH}_3\text{NH}_2$ ) in ethanol at room temperature. Compared to the standard diethyl ether/ethanol purification process, which is commonly used,<sup>1-4</sup> we recrystallized our material three times from hot solutions of ethanol. Finally, we obtained fine and large flakes of highly crystalline MAI that was used as a standard high-purity material. In a 500 mL flask, 27.86 mL  $\text{CH}_3\text{NH}_2$ , 40 % in methanol, were mixed with 100 mL of ethanol. Then, at room temperature, 30 mL 57 % HI (contains  $< 1.5\%$   $\text{H}_3\text{PO}_2$  as stabilizer) in  $\text{H}_2\text{O}$  was added dropwise under continuous stirring. The obtained solution was placed in a rotary evaporator at  $60^\circ\text{C}$  to remove all solvents. Then after several times washing with diethyl ether, MAI was dissolved in ethanol and precipitated twice with diethyl ether. To obtain single crystals, MAI was dissolved in 80 mL of hot ethanol and placed in a refrigerator at  $-3^\circ\text{C}$  for crystallization. Large flakes (up to 7 mm) were obtained. The synthesis of standard methylammonium iodide with diethyl ether purification steps only, which contains a higher level of impurities (low-purity MAI) is described elsewhere.<sup>1-4</sup>

*Methylammonium Hypophosphite Synthesis* ( $\text{MAH}_2\text{PO}_2$ ): 8.7 mL of 50 %  $\text{H}_3\text{PO}_2$  in  $\text{H}_2\text{O}$  was mixed with 100 mL of ethanol. Then 29 mL  $\text{CH}_3\text{NH}_2$  (40 % in methanol) was slowly added under continuous stirring. After 10 min, solvents were extracted by a rotary evaporator at  $60^\circ\text{C}$ . The thus obtained highly viscous liquid was diluted with ethanol, and separated from ethanol by acetone. Small drops of  $\text{CH}_3\text{NH}_3\text{H}_2\text{PO}_2$  were precipitated on the bottom of the flask forming an immiscible biphasic mixture. The washing process by ethanol/acetone mixture was repeated twice. The bottom phase was separated, and dried in vacuum at  $60^\circ\text{C}$  for 1 h. At room temperature,  $\text{CH}_3\text{NH}_3\text{H}_2\text{PO}_2$  is a highly viscous liquid. Methylammonium hypophosphite is highly soluble in polar protic solvents such as methanol, formamide, n-propanol, etc., and well mixable with polar aprotic solvents such as DMF and DMSO.

*Methylammonium Phosphite Synthesis* ( $\text{MAH}_2\text{PO}_3$ ): In a 500 mL flask, 6.3 g of  $\text{H}_3\text{PO}_3$  was dissolved in 20 mL of water and further mixed with 100 mL of ethanol. Then, 29 mL  $\text{CH}_3\text{NH}_2$  (40% in methanol) was slowly added under continuous stirring. After 10 min, solvents were extracted by a rotary evaporator at 60 °C. The highly viscous liquid was diluted with methanol, and small white crystals were precipitated by acetone. Purification was repeated twice, and the highly crystalline white powder was dried in a vacuum oven at 30 °C for 5 h. Higher temperature or longer time of drying led to partial decomposition of the salt, it changed to a light brown color due to  $\text{H}_3\text{PO}_4$  formation. The dried powder is highly soluble in polar protic solvents such as methanol, formamide, n-propanol, etc., but dissolves very poorly in polar aprotic solvents (N,N-dimethylformamide, dimethyl sulfoxide, acetone, acetonitrile, etc.) with only concentrations of up to 1 mg/mL achieved. However, in the presence of  $\text{CH}_3\text{NH}_3\text{H}_2\text{PO}_2$ ,  $\text{CH}_3\text{NH}_3\text{H}_2\text{PO}_3$  is well soluble in DMF or DMSO.

$\text{CH}_3\text{NH}_2$  (40% in methanol) was purchased from ABCR GmbH & Co KG.  $\text{H}_3\text{PO}_2$  solution (50 wt % in water),  $\text{H}_3\text{PO}_3$  (99%), DMF (anhydrous, 99.8%), DMSO (99.9%), ethanol (absolute, 99.8%), and hydroiodic acid (57% in water, contains < 1.5% hypophosphorous acid as stabilizer) were purchased from Sigma-Aldrich. Dimethyl sulfoxide-d6 (DMSO, 99.9 at % D) was purchased from Deutero GmbH.

### 1.1.1 Commercial MAI materials

All commercial MAI materials were bought in August 2016. Ossilla then sold two different purity grades of which we used that which stated 99.9% purity (order number: M271, no batch number given). Sigma Aldrich gave the purity of their MAI as 98% (order number: 793493-5G, Lot number: MKBW1004V). Solaronix did not state a purity value for the MAI they supplied (order number: 24153, batch number: 17/260916FM). Finally Dyesol (now Greatcell Solar Materials) also did not state a purity value (order number: 101000, batch number: 243602) at the time of purchase.

## 1.2 NMR absorption spectra of the precursor

Nuclear magnetic resonance (NMR) measurements were performed to characterise the different MAIs and their purity. The different batches of MAI were dissolved in DMSO-d<sub>6</sub> for the measurement. A Bruker NEO 400 NMR machine was used for the NMR measurements at 400 MHz. As Levchuk et al. have described in detail, NMR spectra are a great tool to characterise the presence of impurities in different MAI batches.<sup>5</sup>

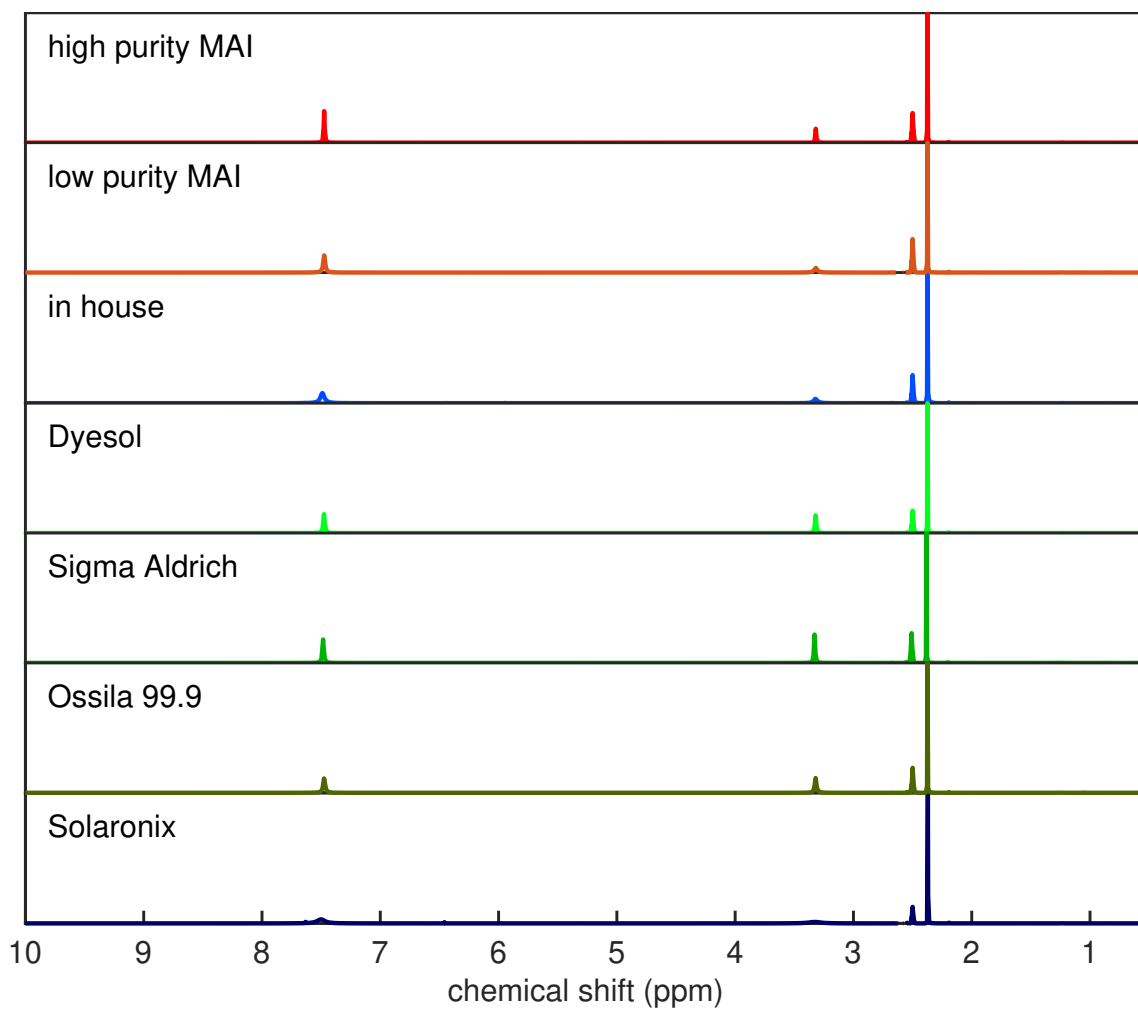


Figure S1: Overview over the <sup>1</sup>H NMR spectra taken of different batches of MAI. Each MAI sample was dissolved in DMSO-d<sub>6</sub> and measured in a Bruker NEO 400 NMR.

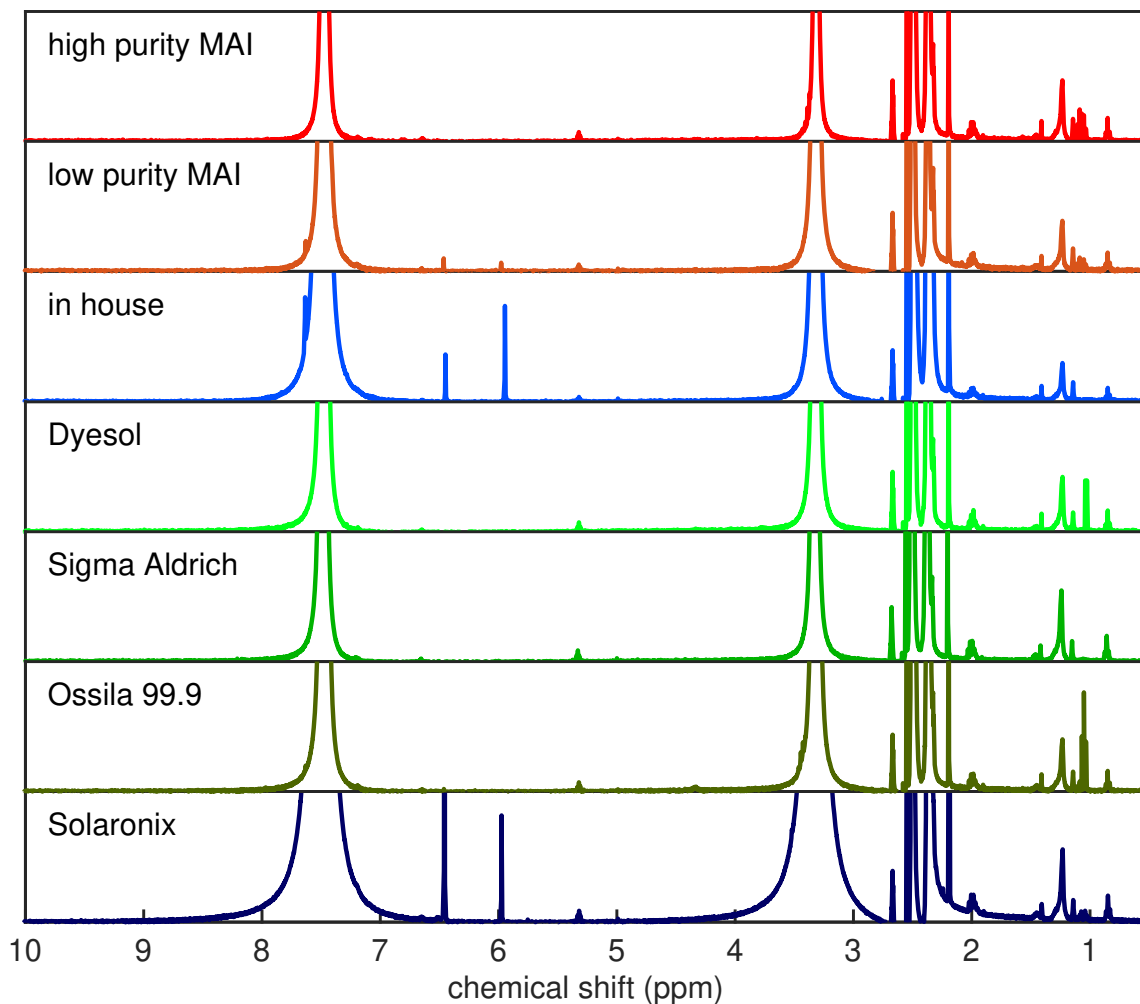


Figure S2: Zoom into the <sup>1</sup>H NMR spectra of different MAI batches. When zooming into the lower counts, additional small peaks which are associated with impurities, are found.

### 1.3 Infra-red absorption spectra of precursors and impurities

To measure the absorption spectrum in the infra-red of the MAI and the isolated impurities MAH<sub>2</sub>PO<sub>3</sub> and MAH<sub>2</sub>PO<sub>2</sub> as well as H<sub>2</sub>PO<sub>3</sub> and H<sub>2</sub>PO<sub>2</sub>, we used a Fourier-transform infra-red spectroscopy (FTIR) set-up with an attenuated total reflectance (ATR) extension. The machine used was a Bruker Vertex 80v interferometer with a Bruker Platinum ATR accessory. The attenuated total reflectance technique makes it possible for us to easily measure the infra-red absorption spectrum of a solid or liquid sample by placing it directly onto the ATR's

diamond crystal.

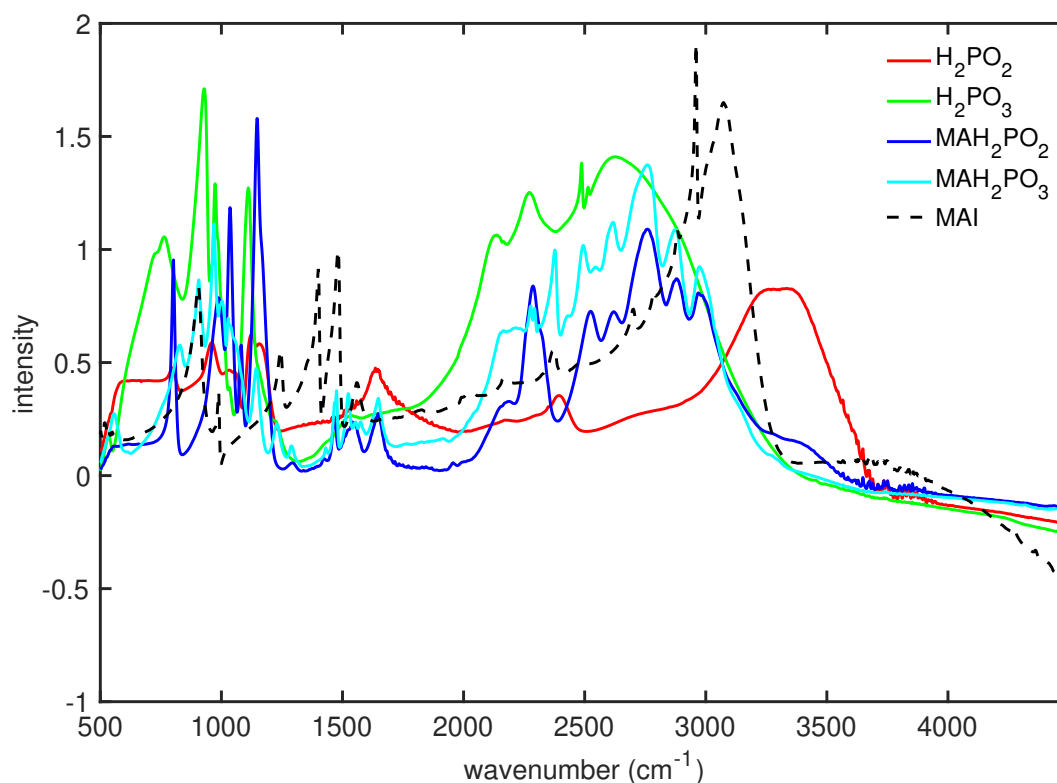


Figure S3: ATR-FTIR infra-red absorption spectra of H<sub>2</sub>PO<sub>2</sub>, H<sub>2</sub>PO<sub>3</sub>, MAH<sub>2</sub>PO<sub>2</sub> and MAH<sub>2</sub>PO<sub>3</sub> as well as methylammonium iodide (MAI). Spectra were taken with a Bruker Vertex 80v interferometer combined with a Bruker Platinum ATR accessory.

#### 1.4 Comparison of the MAI mass spectrometry data with database entry for MA

In Figure S4 we compare the measured mass spectrum for the high-purity MAI batch with the mass spectroscopy spectrum for methylamine (MA) from the NIST database (NIST#: 228024). For masses below 50 AMU/e the two spectra are very similar. All the main peaks from the methylamine spectrum are reproduced in the methylammonium iodide spectrum that we measured.

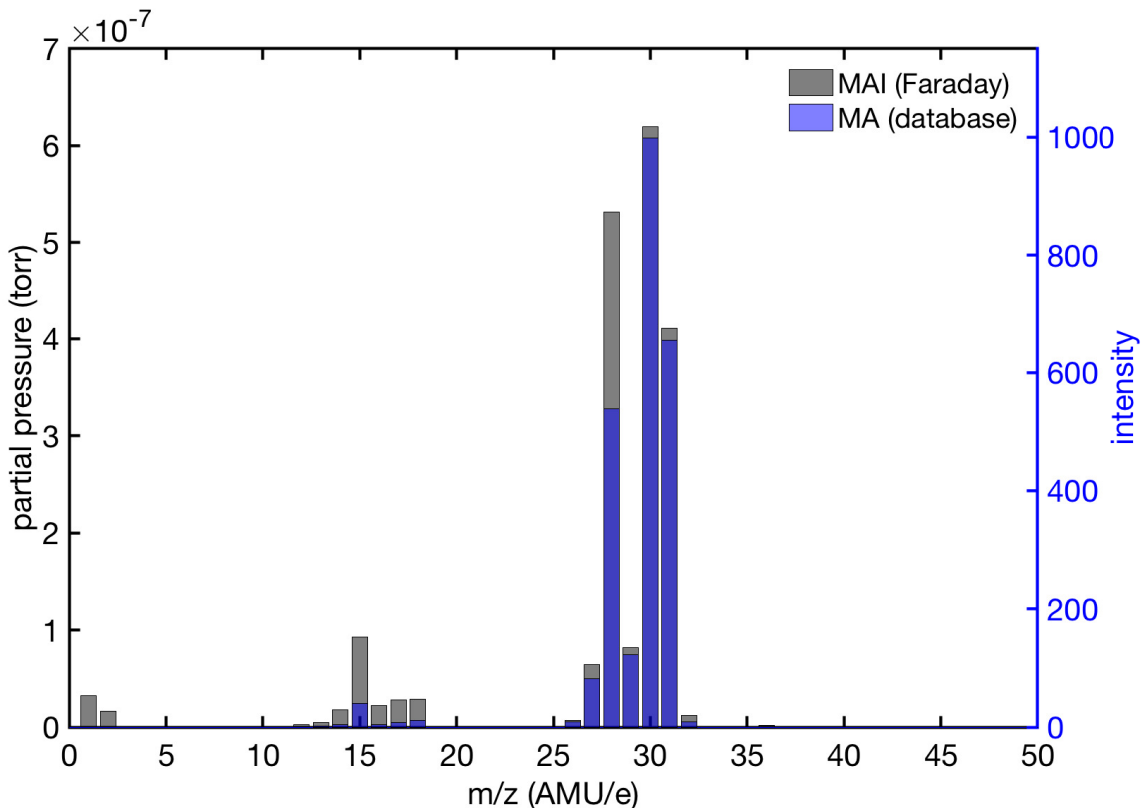


Figure S4: Comparison of the mass spectrum of methylammonium iodide (MAI) (grey) measured with the Faraday detector with the mass spectrum for methylamine (MA) (blue) obtained from the NIST database. The peak positions match well with small deviations in the peak intensities, which are attributed to other constituents in the chamber, such as nitrogen.

We also compared the spectrum from the evaporation of low-purity MAI with the mass spectrum of the isolated impurities, as shown in Figure 2 in the main text. Unfortunately, isolated  $\text{MAH}_2\text{PO}_2$  is liquid at room temperatures and therefore could not be evaporated in our chamber, making it difficult for us to obtain a reference mass spectrum for this material.

## 2 Further Deposition Monitoring

### 2.1 Details of RGA system used

Before the deposition, the vacuum chamber was pumped down to vacuums better than  $5 \times 10^{-6}$  mbar. To monitor the composition of the gas remaining in the chamber during

evaporation we used a residual gas analysis system with a Hiden Analytical quadrupole mass spectrometer. The mass spectrometer is connected to the back of the chamber where it samples the residual gas in the chamber. It contains a filament which ionises the molecules, and two detectors. For the measurements shown in the main article, the Faraday detector was used for the lower masses and the SEM detector for the higher masses. This splitting of the measurement range made it possible for us to optimally use the different capabilities of the detectors. The Faraday detector is more robust and can cope with relatively high pressures but is not sensitive enough for masses that are only present in very small quantities. In contrast, the SEM detector is more sensitive and can pick up masses that are only present in low concentrations, the SEM cannot be used if the partial pressure of the measured mass is too high and it also loses sensitivity over time which makes the application of increasing voltages to the SEM detector necessary to compensate for this. The lower mass range had several strong peaks, for example the nitrogen peak at 28 AMU/e. To avoid damage to the SEM detector this lower range was measured with the Faraday detector and the higher masses, where more sensitivity was needed, were measured with the SEM detector. The ranges for each of the detectors were chosen so that there was a small overlap of masses that were measured by both detectors. These masses were later used to correct for differences in the partial pressures measured by the two different detectors.

## **2.2 Infra-red spectra of deposits on quartz micro balance crystals**

In the evaporation chamber three quartz micro balances are mounted, one each close to the MAI source, the  $\text{PbI}_2$  source and the substrate. To check if the MAI batch used made any chemical difference to the deposited materials, we performed attenuated total reflectance infra-red measurements (ATR Infra-red) on the quartz crystals. Fresh gold coated quartz crystals were installed in each balance before the deposition. They were removed after the deposition and measured with a Bruker Vertex 80v interferometer with a Bruker Platinum ATR accessory. A built-in anvil was used to press the crystal surface directly against the

ATR's diamond crystal. Some of the data from these measurements are shown in Figure 4c in the main text. In addition we here show all the data obtained.

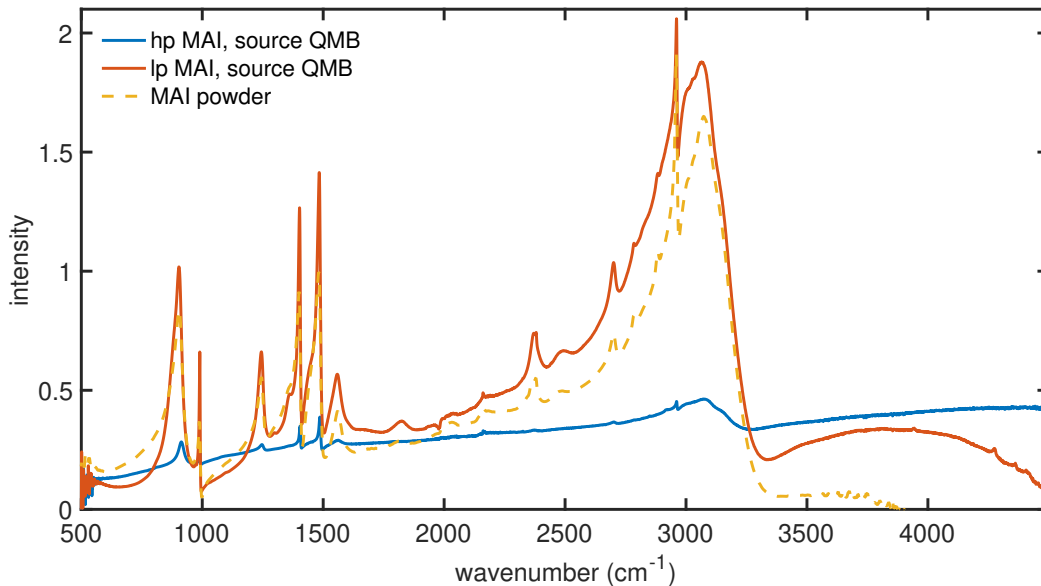


Figure S5: ATR infra-red absorption spectra of the QMB placed close to the MAI source during deposition with high-purity MAI (blue), and low-purity MAI (red). For comparison the data for high-purity MAI powder is shown as well (dashed line).

The infra-red absorption spectrum from the QMB crystal that was mounted next to the MAI source during the deposition with low-purity MAI is very similar to the spectrum of the high-purity MAI powder, with all of the expected features present. For the QMB used during the deposition with the high-purity MAI the signal is overall much weaker but the main features can still be seen. These observations are consistent with less material adhering to the QMB in this deposition, which matches our observations in cross-sectional SEM measurements (compare Figure 4 in the main text).

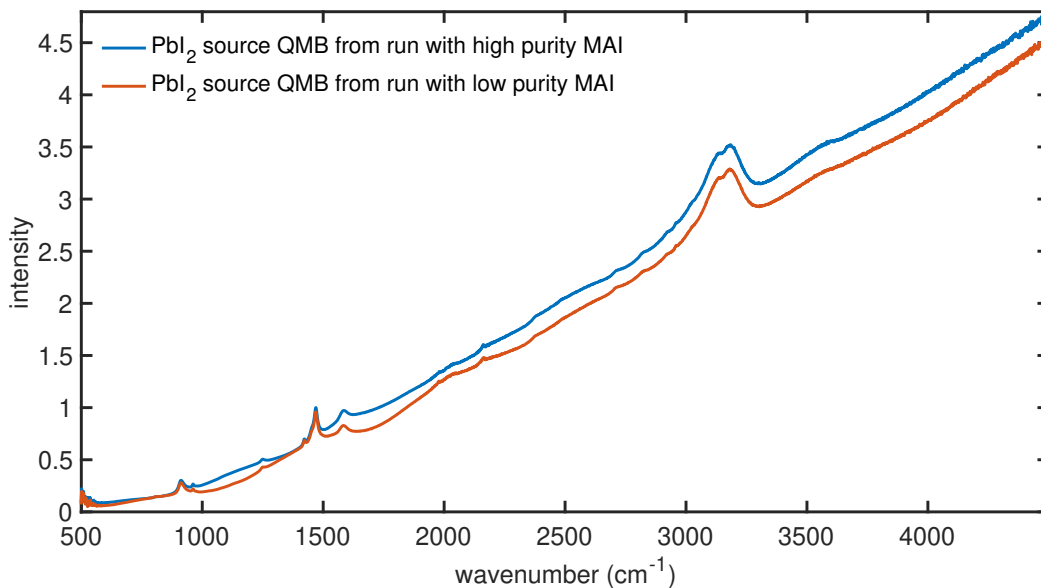


Figure S6: ATR infra-red absorption spectra of the QMB placed close to the PbI<sub>2</sub> source during co-evaporation with high-purity MAI (blue), and low-purity MAI (red).

The infra-red absorption spectra of the material deposited onto the QMBs which were mounted close to the PbI<sub>2</sub> source are nearly identical. The small difference in intensity can be explained by small differences of how firmly the QMB is pressed against the ATR crystal. This strong similarity is expected, as the QMB monitors at the PbI<sub>2</sub> source are only meant to detect the PbI<sub>2</sub> and not the MAI. Therefore a change in MAI batch should not influence the deposition on this QMB crystal.

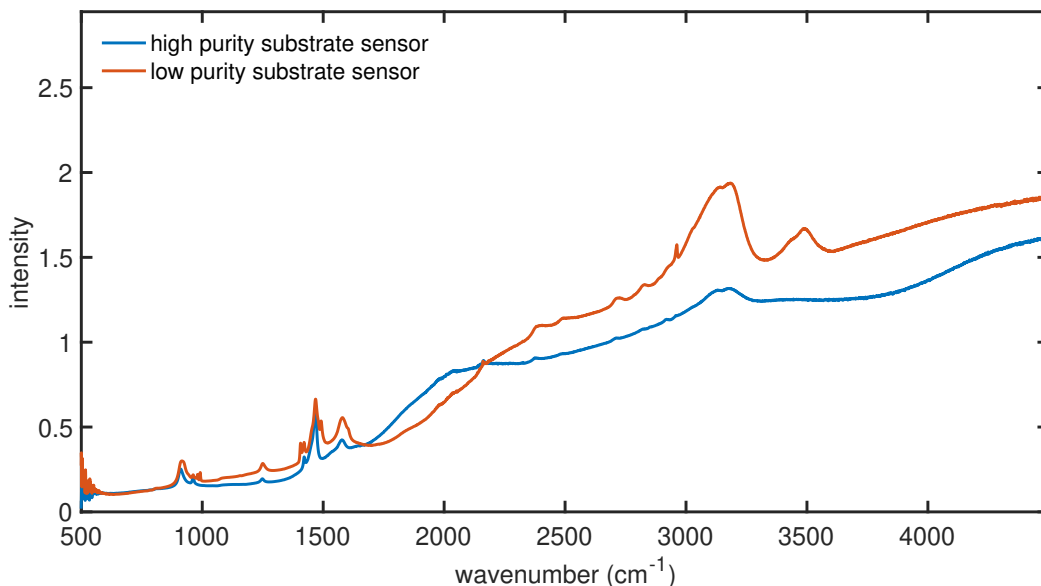


Figure S7: ATR infra-red absorption spectra of the QMB placed close to the substrate during co-evaporation with high-purity MAI (blue), and low-purity MAI (red).

Finally we investigate the infra-red spectra of the QMB monitors mounted next to the substrate, and find these to be broadly similar.

### 2.3 PID control of the source temperatures

The temperature of the thermal sources and therefore the evaporation and subsequent deposition of the precursors is controlled with proportional–integral–derivative (PID) controllers. These can be set to either maintain a constant rate or to a constant temperature. In this study the PID controlling the MAI was typically set to a constant temperature and the one controlling the  $\text{PbI}_2$  source was set to maintain a constant rate on the QMB mounted near that source. The PID values for the  $\text{PbI}_2$  source were carefully tuned to achieve a smooth and constant evaporation of the  $\text{PbI}_2$ . This process was successful as can be seen in the  $\text{PbI}_2$  source temperature curve in Figure S8, which is very smooth. In contrast, the PID values for MAI were slightly detuned which lead to a small oscillation of the MAI source temperature. This approach was utilized to identify the contributions from MAI in other measurements such as the RGA and QMB measurements.

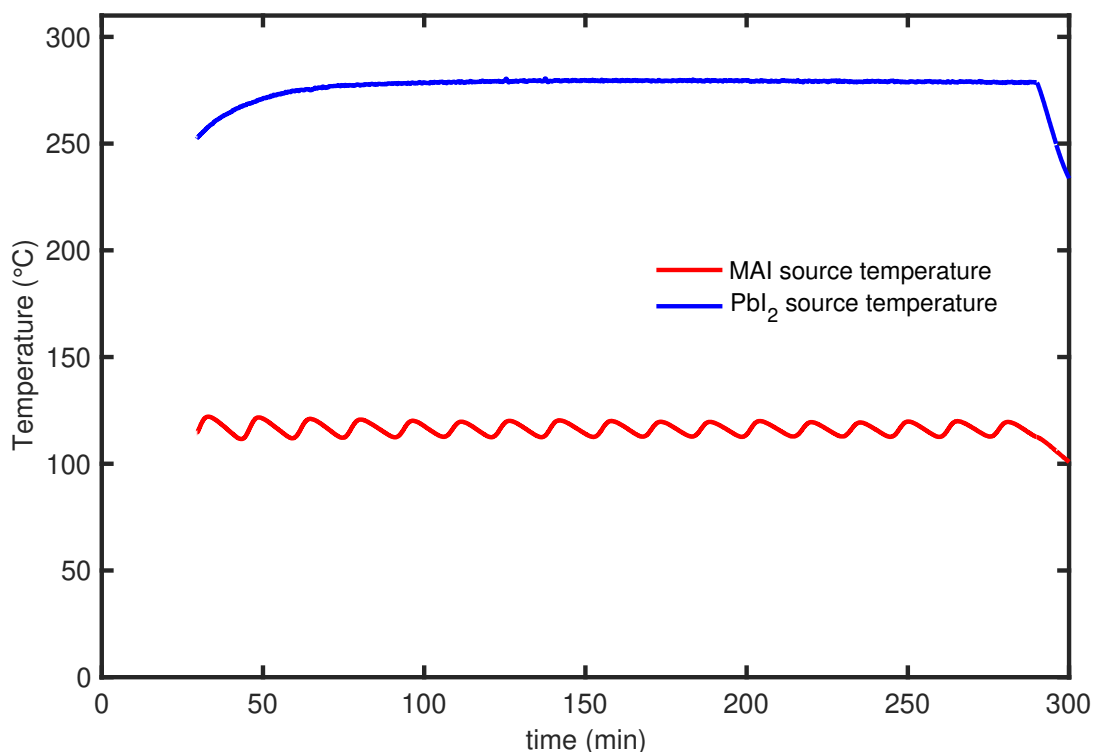


Figure S8: Source temperatures of the MAI source (red) and PbI<sub>2</sub> source (blue) over the course of an exemplary co-evaporation run.

## 2.4 Rate-controlled evaporation run with high-purity MAI

It was not possible to use the quartz micro balance (QMB) to control the deposition run with the high-purity MAI. To demonstrate clearly the problem, we set-up a standard evaporation run controlled with the QMB. We set the MAI rate to a typical value and let the PID controller try to regulate the evaporation using the apparent rate the QMB measured. To maintain this apparent rate, the controller continued to increase the temperature until it got well above the normal evaporation temperature (around 120°C). It appears that the QMB was not registering enough MAI and therefore the PID controller kept increasing the temperature. The temperature kept rising until eventually the MAI in the crucible ran out. This is apparent in Figure S9 after about 55 min when the temperature continues to rise but the apparent rate on the QMB drops off completely.

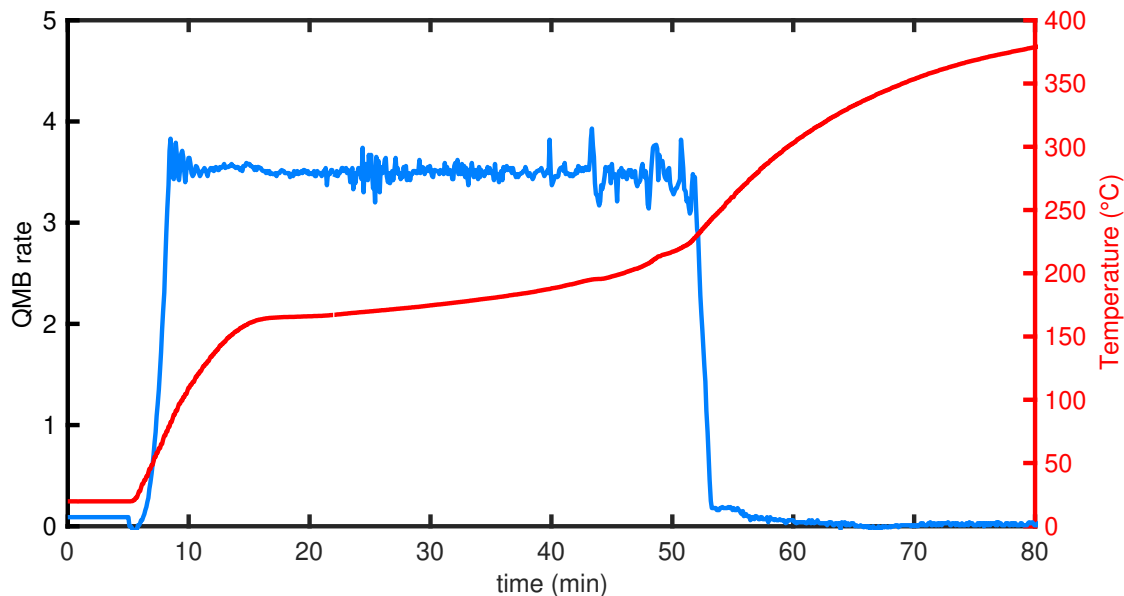


Figure S9: A standard rate controlled evaporation run is set-up with the high-purity MAI as the organic precursor. The development of the temperature and the QMB reading are shown and demonstrate that the rate control is unsuccessful and the MAI runs out during the evaporation.

### 3 Further Thin-Film characterisation

#### 3.1 X-Ray Diffraction

X-ray diffraction (XRD) measurements were performed with a Panalytical X'pert powder diffractometer. A standard  $\theta - 2\theta$  scan was performed on one MAPbI<sub>3</sub> thin-film sample for each MAI batch. Both for the low-purity MAI and the high-purity MAI a sample from the batch that contained the champion solar cell was used for the XRD. The two XRDs are very similar. Both show a very small peak around 12.6°, indicating a small amount of PbI<sub>2</sub> in the film. Otherwise the expected peaks for MAPbI<sub>3</sub> are clearly visible in both samples, for example at 14° and 28°.

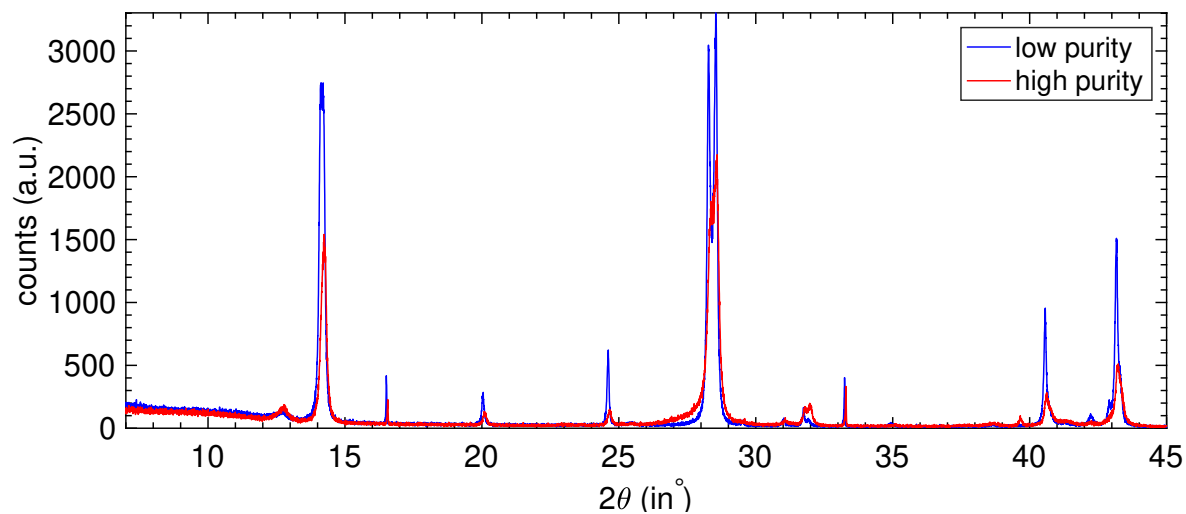


Figure S10: XRD spectra measured with a Panalytical X'pert powder diffractometer for samples from MAPbI<sub>3</sub> deposition runs performed with low-purity MAI (blue) or high-purity MAI (red).

### 3.2 Scanning Electron Microscopy

Cross-sectional scanning electron microscopy (SEM) images were taken using a FEI Quanta 600 FEG. MAPbI<sub>3</sub> thin-films were deposited onto glass which was coated with fluoride-doped tin oxide (FTO). The substrates were then broken in half and mounted vertically to enable recording of SEM images of the cross-section.

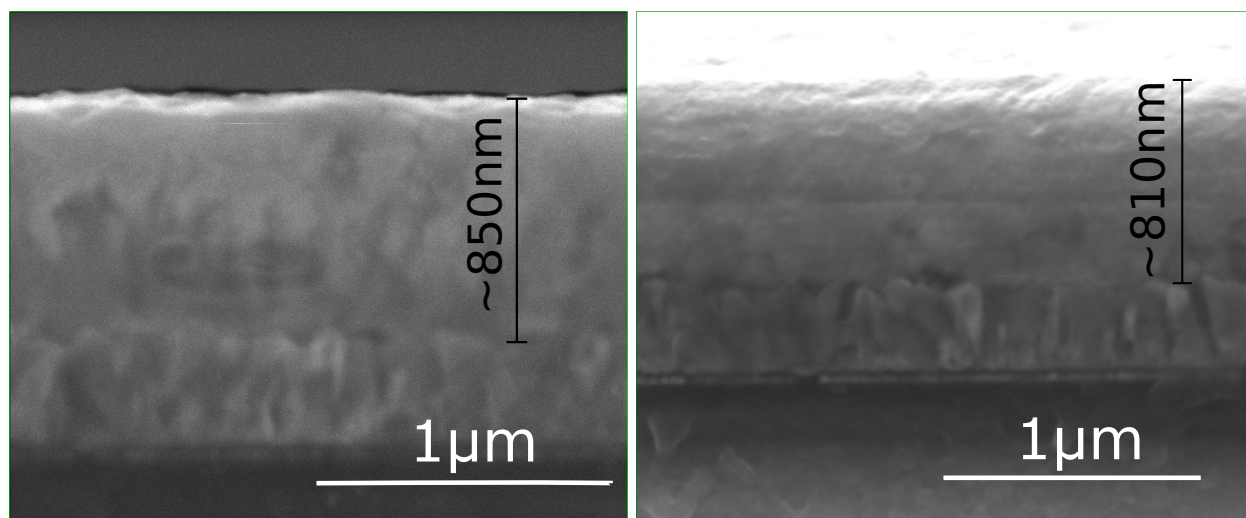


Figure S11: Scanning electron micrographs of a  $\text{MAPbI}_3$  thin-film deposited in the same run as the champion solar cell. On the left the perovskite film was deposited with the low-purity MAI on the right a perovskite film deposited with the high-purity MAI.

## 4 Further Device Information

### 4.1 Device architecture

To fabricate the solar cells a standard layout was used. The substrate was float glass coated with fluoride-doped tin oxide (FTO). A thin layer of  $\text{C}_{60}$  was evaporated on top. The  $\text{C}_{60}$  deposition was carried out in the same evaporation chamber as the later perovskite deposition. The  $\text{MAPbI}_3$  layers were co-evaporated as described in the main article and above in section 2. As Figure S11 shows, the thickness of the perovskite layer in the champion devices was between 810 nm and 850 nm. On top a layer of Spiro-OMeTAD was spin-coated from a solution of 73 mg/ml Spiro-OMeTAD in chlorobenzene with a spinspeed of 2000 rpm for 45 s. To dope the Spiro-OMeTAD, 38  $\mu\text{l}$  of 170 mg/ml lithium bis(trifluoromethanesulfonyl)imide (LiTFSi) in 1-Butanol were added as well as 21  $\mu\text{l}$  of 4-tert-butylpyridine. This layer stack was then left in a dry atmosphere overnight before 100 nm of silver were evaporated with a Lesker Nano36 evaporator to finish the solar cell.

## 4.2 Device Optimization

To optimize the efficiency of the solar cells we varied the deposition time and therefore the thickness of the MAPbI<sub>3</sub> absorber layer. Below the champion efficiency from each evaporation run is shown. The optimal deposition time when using the high-purity MAI was higher than when the low-purity MAI was used. But the SEM (Figure S11) shows, that despite this difference, the thickness for the two best solar cells was the same.

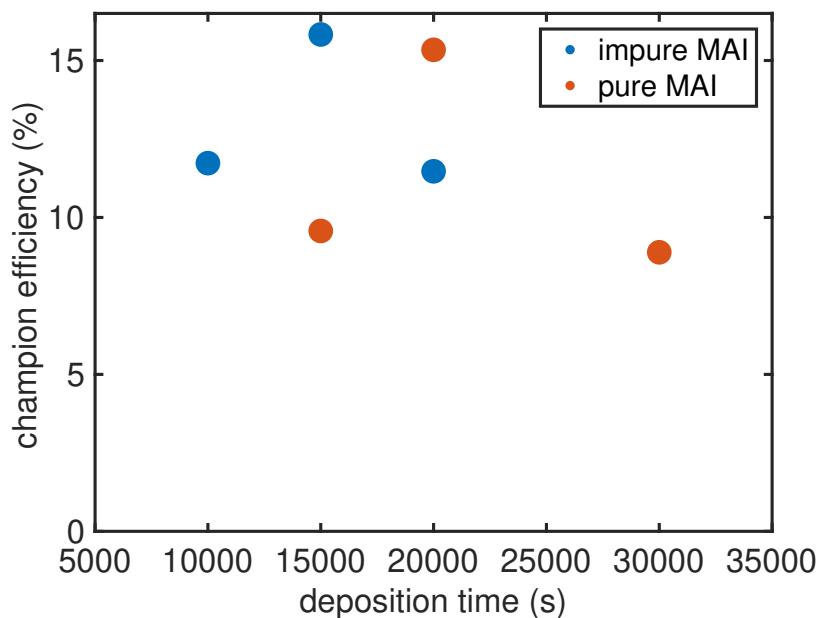


Figure S12: Deposition time optimisation for co-evaporations using two different MAI batches. Low-purity MAI in blue and high-purity MAI in red. Nearly the same champion efficiency is reached but after different deposition times.

## 4.3 Spread of efficiencies for champion batches

As a result of the thickness optimizations, nearly equal champion efficiencies were achieved with both high-purity and low-purity MAI. To show the cell performance beyond the champion device, the scanned efficiencies of all the cells of the batches that included the champion cell are plotted in histograms. The only noteworthy difference can be found in the higher number of solar cells that completely failed in the batch made with low-purity MAI.

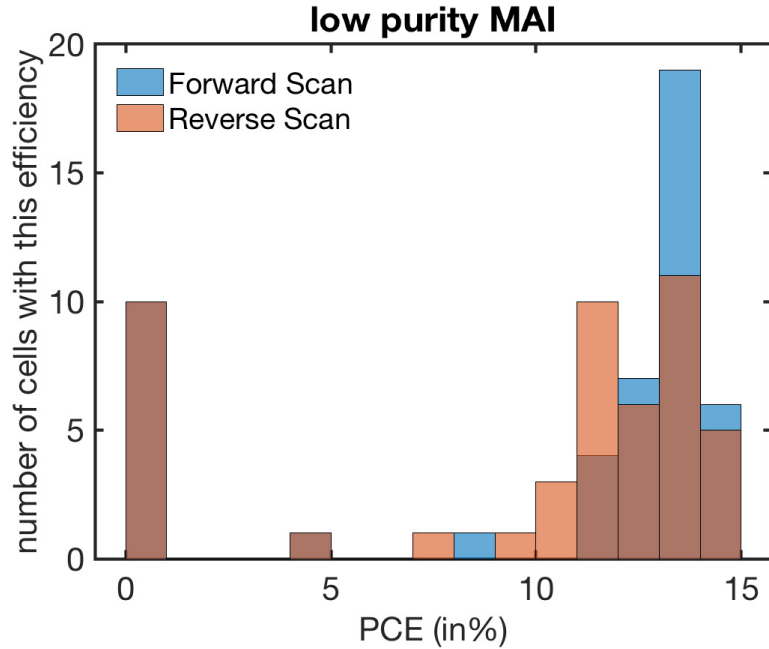


Figure S13: Power conversion efficiencies of all cells produced in the same batch as the champion solar cell for low-purity MAI. A large number of cells reach high efficiencies of up to 15%.

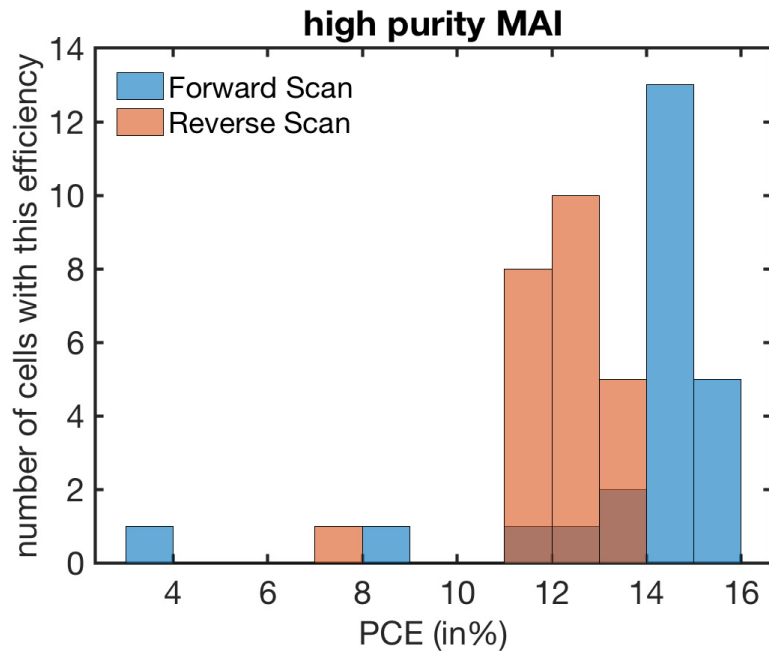


Figure S14: Power conversion efficiencies of all cells produced in the same batch as the champion solar cell for high-purity MAI. A large number of cells reach high efficiencies of around 15%.

#### 4.4 Stabilized power output measurement

For the J-V sweeps and the stabilized power output measurements (SPO) an ABET class AAB Sun 2000 simulator was used. Black masks were used to achieve a well-defined active area and to prevent influences from light scattering. Hysteresis in the J-V curves of perovskite solar cells has been a commonly observed phenomenon. To obtain reliable efficiency measurements independently of possible hysteresis, stabilized power output (SPO) measurements are being used. For these measurements the solar cell is held close to the maximum power point (MPP) for 50s while the current and efficiency is measured. The SPO curves for both the champion device fabricated with low-purity MAI and with high-purity MAI are shown below. The SPOs are very similar for both MAI batches.

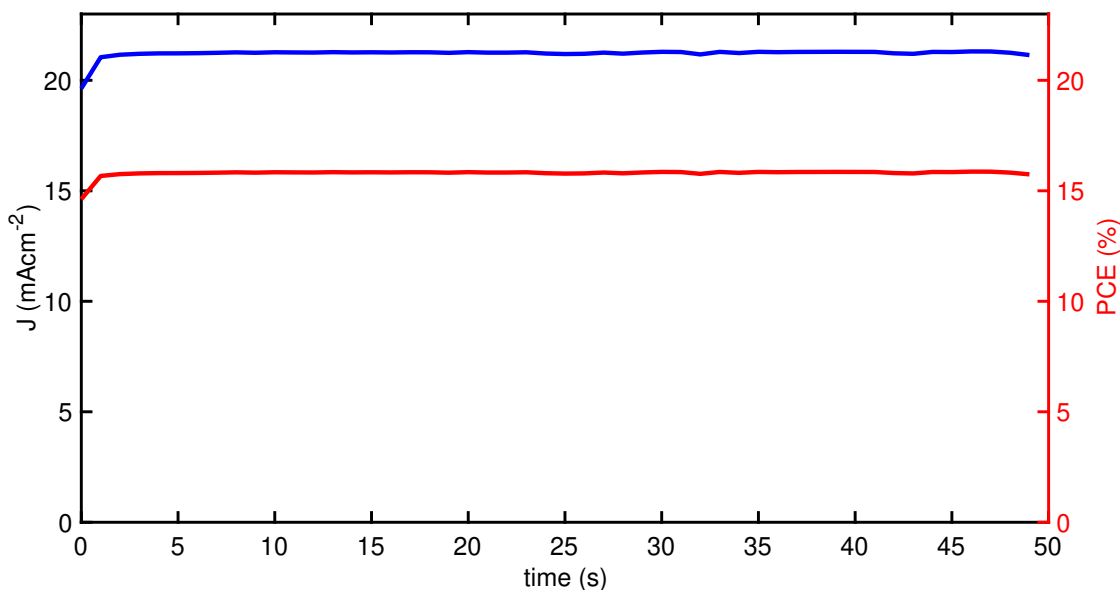


Figure S15: Stabilized power output of the champion cell from the best deposition run with low-purity MAI.

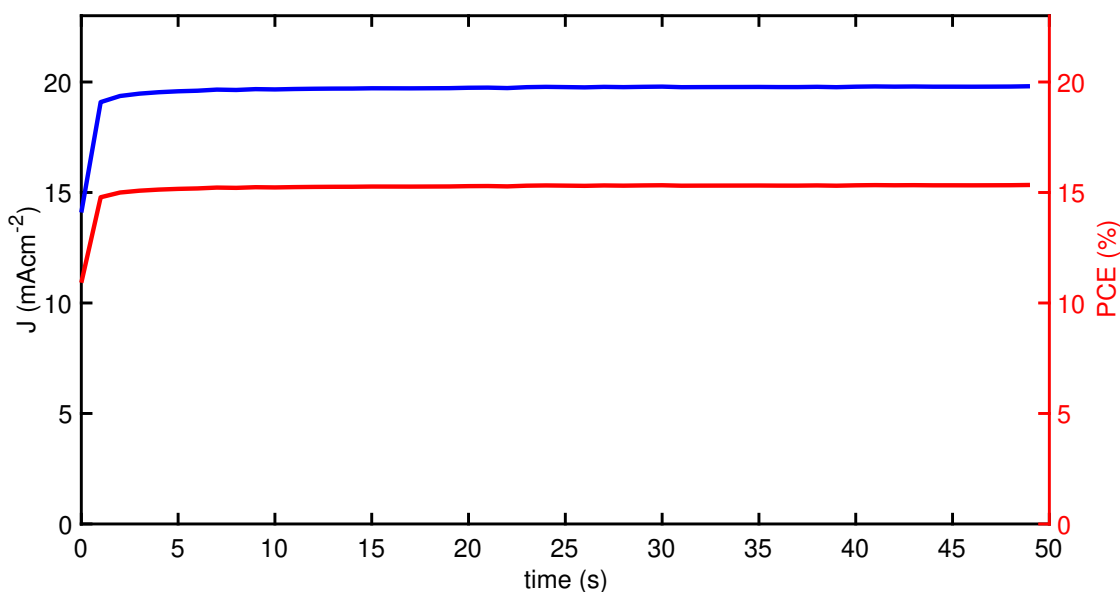


Figure S16: Stabilized power output of the champion cell from the best deposition run with high-purity MAI.

## References

- (1) Kojima, A.; Teshima, K.; Shirai, Y.; Miyasaka, T. Organometal Halide Perovskites as Visible-Light Sensitizers for Photovoltaic Cells. *Journal of the American Chemical Society* **2009**, *131*, 6050–6051.
- (2) Lee, M. M.; Teuscher, J.; Miyasaka, T.; Murakami, T. N.; Snaith, H. J. Efficient Hybrid Solar Cells Based on Meso-Superstructured Organometal Halide Perovskites. *Science (New York, N.Y.)* **2012**, *338*, 643–637.
- (3) Zhang, W.; Pathak, S.; Sakai, N.; Stergiopoulos, T.; Nayak, P. K.; Noel, N. K.; Haghighirad, A. A.; Burlakov, V. M.; DeQuilettes, D. W.; Sadhanala, A.; Li, W.; Wang, L.; Ginger, D. S.; Friend, R. H.; Snaith, H. J. Enhanced Optoelectronic Quality of Perovskite Thin Films with Hypophosphorous Acid for Planar Heterojunction Solar Cells. *Nature Communications* **2015**, *6*, 10030.

- (4) Yan, K.; Long, M.; Zhang, T.; Wei, Z.; Chen, H.; Yang, S.; Xu, J. Hybrid Halide Perovskite Solar Cell Precursors: Colloidal Chemistry and Coordination Engineering behind Device Processing for High Efficiency. *Journal of the American Chemical Society* **2015**, *137*, 4460–4468.
- (5) Levchuk, I.; Hou, Y.; Gruber, M.; Brandl, M.; Herre, P.; Tang, X.; Hoegl, F.; Bartschuk, M.; Osvet, A.; Hock, R.; Peukert, W.; Tykwinski, R. R.; Brabec, C. J. Deciphering the Role of Impurities in Methylammonium Iodide and Their Impact on the Performance of Perovskite Solar Cells. *Advanced Materials Interfaces* **2016**, 1600593.